THE JOURNAL OF PHYSICAL CHEMISTRY C

Article

pubs.acs.org/JPCC

Crystallization of $HC(NH_2)_2PbI_3$ Black Polymorph by Solvent Intercalation for Low Temperature Solution Processing of Perovskite Solar Cells

Congcong Wu,*,† Xiaojia Zheng,*,† Qiang Yang,† Yongke Yan,† Mohan Sanghadasa,‡ and Shashank Priya*,†

†Center for Energy Harvesting Materials and System (CEHMS), Virginia Tech, Blacksburg, Virginia 24061, United States

‡Aviation and Missile Research, Development, and Engineering Center, US Army RDECOM, Redstone Arsenal, Alabama, United States

S *Supporting Information*

ABSTRACT: One of the critical problems in fabrication of flexible perovskite modules and resolving their reliability issue remains the necessity to utilize high temperature annealing for synthesis of perovskite and electron transport layers. Here, we provide a breakthrough in addressing these challenges by demonstrating low temperature synthesis of both of these layers. $HC(NH)_2PbI_3$ (commonly known as $FAPbI_3$) has two polymorphs, a high temperature-stable black $FAPbI_3$ perovskite-type pseudocubic polymorph (α-phase) and a low temperature-stable yellow non-perovskite hexagonal polymorph (δ-phase). In order to understand the crystallization kinetics of the $FAPbI_3$ black polymorph, a PbI_2-NMP complex is fabricated via solvent intercalation between the adjacent I-Pb-I layers. Utilizing structural, electrical, and thermal analyses, the connection between solvent intercalation and the crystallization of the $FAPbI_3$ black polymorph is established. It is found that the solvent intercalation in the PbI_2 crystal causes lattice strain and the induced strain energy could reduce the activation barrier of the intermediate state and favor the crystallization of the $FAPbI_3$ black polymorph. The TiO_2 compact layer with a smooth surface, high crystallinity, and superior electron transport is also fabricated at room temperature by using a TiO_2 slurry composed of volatile solvents and TiO_2 nanoparticles. Using low temperature solution processed TiO_2 as electron transport layer, the $FAPbI_3$-based perovskite solar cell exhibits a conversion efficiency of 13.2% with significantly reduced hysteresis effect, benefiting from the low electron and hole trap state density. The low temperature process developed in this study holds great promise for flexible perovskite solar cells and perovskite tandem solar cells.

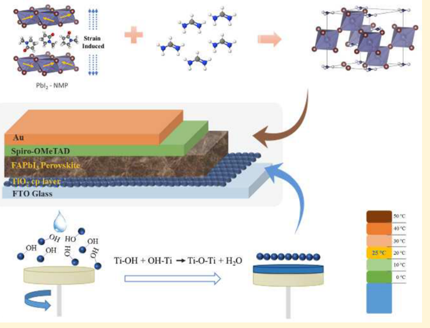

1. INTRODUCTION

The emergence of the inorganic−organic hybrid halide perovskite solar cell (PSC) is regarded as a significant breakthrough in photovoltaic technology, promising low-cost and high-performance solar cells.[1−3] Despite the process and efficiency advantages, the critical challenges encountered in PSCs are the stability issues including thermal stability, phase stability, and chemical stability. The most commonly used perovskite in PSCs is $CH_3NH_3PbI_3$ ($MAPbI_3$), which has been shown to decompose at ∼85 °C[4] and undergo a phase transition from tetragonal to cubic at ∼55 °C.[5,6] Recently, $HC(NH)_2PbI_3$ ($FAPbI_3$) was suggested as an alternative to $MAPbI_3$ due to its high thermal resistivity, superior light absorption, and enhanced carrier transport.[7−10] Unfortunately, the black $FAPbI_3$ perovskite-type polymorph (α-phase) is only stable at a relatively high temperature over 160 °C, and at room temperature, it converts into a yellow non-perovskite hexagonal polymorph (δ-phase) under ambient air.[6,11] This suggests that the stabilization of the $FAPbI_3$ perovskite black polymorph at room temperature is crucial for achieving stable PSCs. Recently, composition engineering by incorporating mixed cation or halide has proven to be an effective method to stabilize the $FAPbI_3$ black polymorph. Jeon et al. reported that incorporation of $MAPbBr_3$ into $FAPbI_3$ could effectively stabilize the black $FAPbI_3$ perovskite and improve the conversion efficiency to more than 18%.[11] Other cation and halides such as Cs, MA, FACl, and MACl have also been reported to modulate the crystallization of black $FAPbI_3$ perovskite.[10,12−14] Besides composition manipulation strategies, solvent chemistry has been recently explored to modify the formation of the perovskite layer. Liang et al. utilized a solvent additive of 1,8-diiodooctane (DIO) in precursor solution to improve the crystallization of the perovskite layer. They hypothesized that the additive interacts with Pb^{2+} ion and modulates the crystallization kinetics of perovskite.[15] Wang et al. reported that $FAPbI_3$ perovskite prepared from $HPbI_3$ shows a much purer crystalline phase with strong (110) preferred orientation. It was proposed that intercalation of H^+ in PbI_2 crystals slows

Received: October 24, 2016
Revised: October 31, 2016
Published: November 2, 2016

DOI: 10.1021/acs.jpcc.6b10730
J. Phys. Chem. C 2016, 120, 26710−26719

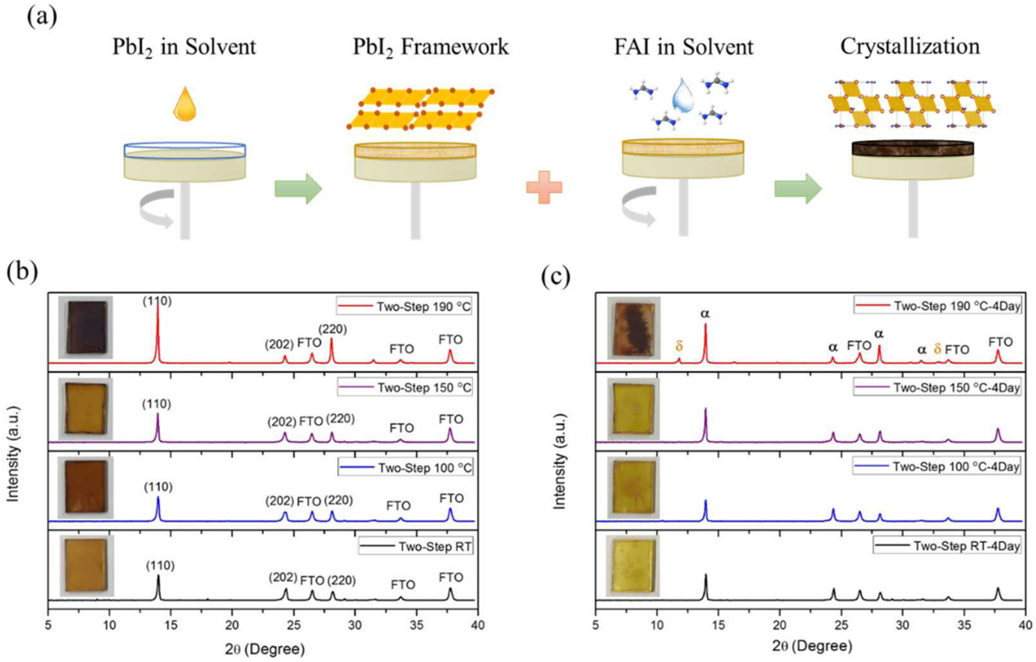

Figure 1. (a) Schematics of one-step synthesis reaction and two-step synthesis reaction. X-ray diffraction (XRD) pattern of $FAPbI_3$ layers prepared through two-step synthesis method at different temperatures (b) before and (c) after 4 day storage in ambient air.

down the reaction and release of excess I^- affects the crystallization kinetics.[16] Yang et al. reported the synthesis of a PbI_2(DMSO) complex, and through intramolecular exchange between DMSO and FAI, the conversion efficiency of the $FAPbI_3$-based PSC was improved to over 20%.[17] Although various solvent additives have been employed to modulate the synthesis of perovskites, the underlying mechanism governing the effect of solvent interaction on the crystallization of the perovskite layer is less understood.

The perovskite layer in PSCs could be fabricated at low temperature by the facile solution-based process. In contrast, the most commonly used TiO_2 electron transport layer needs high temperature process (~500 °C) in order to obtain requisite crystallinity and high electron transport. The high temperature annealing process precludes the utilization of temperature-sensitive substrates, such as polymer substrates and silicon solar cells, thereby limiting the development of flexible PSCs and monolithic perovskite tandem solar cells. To realize a low temperature synthesis process for the TiO_2 electron transport layer, Kim et al. fabricated a compact TiO_x layer by using the atomic layer deposition (ALD) technique. The flexible PSC exhibited a conversion efficiency of 12.2%.[18] Yang et al. fabricated an amorphous TiO_2 layer using DC magnetron sputtering at room temperature, and a high efficiency of 15.07% was obtained for the flexible PSC.[19] PSCs hold an advantage over silicon solar cells in providing a simple and cost-effective process, but the preparation of the TiO_2 layer by the vacuum deposition technique increases the cost and complexity for PSC manufacturing. Thus, low-cost, low temperature techniques for preparation of high efficiency PSCs are still missing.

In this study, we synthesized PbI_2-DMSO and PbI_2-NMP complexes via the solvent intercalation process and investigated the effect of solvent interaction on the crystallization of $FAPbI_3$ perovskites. It was found that the solvent intercalation leads to lattice expansion along the *c*-axis and induces lattice strain in PbI_2 crystal. During the formation of $FAPbI_3$, the release of strain energy in PbI_2 crystals favors the crystallization of the $FAPbI_3$ black polymorph. Further, we developed a solution processed TiO_2 compact layer with high crystallinity and density at room temperature. The $FAPbI_3$-based PSC was prepared by using the room temperature fabricated TiO_2 film as the electron transport layer. The low temperature $FAPbI_3$-based PSC shows reduced hysteresis, with a reverse-scan efficiency of 13.2% and forward-scan efficiency of 11.8%.

2. EXPERIMENTAL SECTION

2.1. Materials. Fluorine-doped tin oxide (FTO) glass was purchased from Nippon Sheet Glass; TiO_2 paste (18NR-T) was from Dyesol; TiO_2 sol paste (Ti-Nanoxide T-L) was obtained from Solaronix; PbI_2 (99.99%) was purchased from Alfa-Aesar; and $HC(NH_2)_2I$ (FAI), CH_3NH_3Br (MABr), CH_3NH_3I (MAI), 2,2′,7,7′-tetrakis(*N*,*N*-di-4-methoxyphenyl-amino)-9,9′-spirobifluorene (Sprio-OMeTAD), and Co(III) TFSI salt (FK209) were obtained from Luminescence Technology Corp. Dimethylsulfoxide (DMSO), *N*-methyl-2-pyrrolidone (NMP), *N*,*N*-dimethylformamide (DMF), titanium isopropoxide (TTIP), *tert*-butyl alcohol, toluene, chlorobenzene, α-terpineol, 2-propanol, ethanol, and acetonitrile were purchased from Sigma-Aldrich.

2.2. Synthesis of PbI_2 Complex Solution. For preparation of PbI_2(DMSO) powder, 5 g of PbI_2 was dissolved in 20 mL of DMSO, and then 40 mL of toluene was added into PbI_2 solution and stirred for 2 h. The generated white precipitation was filtered and dried in vacuum oven for 3 days. Then, 1.3 M PbI_2(DMSO) complex powder was dissolved in DMF to form PbI_2(DMSO) solution. For the solution-based preparation of PbI_2 complex, PbI_2-DMSO solution was fabricated by dissolving 1.3 M PbI_2 and 1.3 M DMSO in DMF; PbI_2-NMP solution was fabricated by dissolving 1.3 M PbI_2 and 1.3 M NMP in DMF.

2.3. Device Fabrication. Low temperature binder-free TiO_2 slurry was prepared by mixing Ti-Nanoxide T-L paste with DI water and *tert*-butyl alcohol, followed by stirring for 2 h

DOI: 10.1021/acs.jpcc.6b10730
J. Phys. Chem. C 2016, 120, 26710−26719

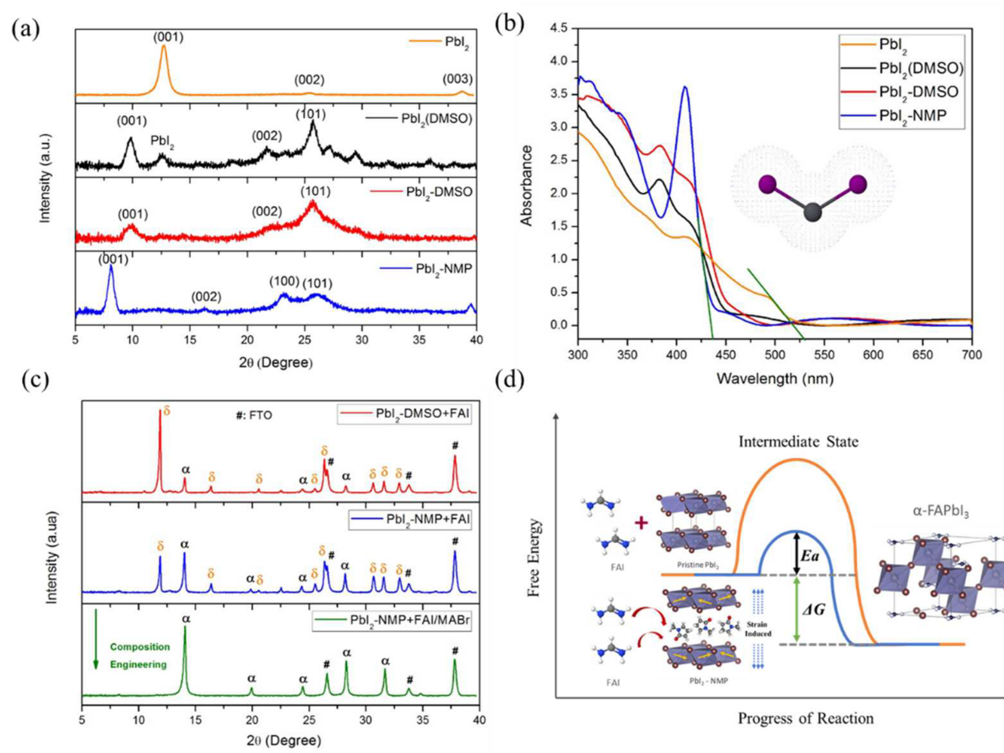

Figure 2. (a) XRD and (b) UV−vis absorbance spectra of pristine PbI_2, PbI_2(DMSO), PbI_2-DMSO, and PbI_2-NMP. (c) XRD of $FAPbI_3$ perovskite layer synthesized by PbI_2-DMSO, PbI_2-NMP, and mixed composition $FAPbI_3$ perovskite synthesized by PbI_2-NMP, annealed at 100 °C for 10 min. (d) Illustration of reaction progress between PbI_2 complex and FAI.

and ultrasonic dispersing for 30 min. The low temperature solution processed TiO_2 compact layer was fabricated by spin-coating TiO_2 slurry at the speed of 6000 rpm for 30 s and drying at room temperature. The conventional TiO_2 compact layer was synthesized through spin-coating mildly acidic TTIP solution at 2000 rpm for 20 s, followed by annealing at 500 °C for 1 h. For a mesoporous architecture, TiO_2 paste prepared by diluting 18NR-T paste with α-terpineol and ethanol was spin-coated on the top of the TTIP TiO_2 compact layer, followed by annealing at 500 °C for 1 h. The $FAPbI_3$ perovskite layer was fabricated via a two-step method. First, PbI_2 complex solution was spin-coated on the TiO_2 electron transport layer at 3000 rpm for 20 s, followed by spin-coating of 465 mM FAI solution in 2-propanol on the PbI_2 complex film at 4000 rpm for 20 s. For the mixed composition $FAPbI_3$ perovskite, 15 mol % of MABr and 85 mol % of FAI were dissolved in 2-propanol, and the mixture was spin-coated on top of the PbI_2 complex film at 4000 rpm for 20 s. The annealing process was completed by heating the sample on a hot plate at 100 or 150 °C for 10 min. Spiro-OMeTAD solution was prepared by dissolving 90 mg of spiro-MeOTAD in 1 mL of chlorobenzene, followed by mixing 45 μL of Li-TFSI/acetonitrile (170 mg/mL), 75 μL of FK209/acetonitrile (100 mg/mL), and 10 μL of 4-*tert*-butylpyridine (TBP). Then, Spiro-OMeTAD solution was spin-coated on the perovskite layer at 4000 rpm for 20 s. Lastly, 80 nm of gold was thermally evaporated as the metal electrode, keeping the active area of each device at 0.096 cm^2.

2.4. Characterization. UV−vis absorption spectra were recorded by a UV−vis spectrophotometer (U-4100, Hitachi). X-ray diffraction (XRD) patterns were measured by a Philips Xpert Pro X-ray diffractometer (Almelo, The Netherlands). The morphology of the film was examined by scanning electron microscopy (SEM, Quanta 600 FEG, FEI). Atomic force microscopy (AFM) was performed using a scanning probe station (Bruker Dimension Icon, USA). Raman spectra were measured using a LabRam HR (JY Horiba) equipped with a 514.53 nm laser. A solar simulator (150 W Sol 2ATM, Oriel) was employed to provide air mass (AM 1.5) illumination of 100 mW cm^{-2}. A Keithley digital source meter (Model 2400) was employed to provide linear potential sweep. *J*−*V* characteristics of the solar cells were measured by both of reverse scan and forward scan.

3. RESULTS AND DISCUSSION

The solution-based techniques for perovskite fabrication can be divided into one-step and two-step syntheses. In a typical one-step synthesis, the perovskite layer is deposited from the precursor solution, whereas the two-step synthesis involves first deposition of the PbI_2 layer and then conversion into perovskite during the sequential step deposition, as illustrated in Figure 1a. Owing to the solid framework of PbI_2 crystal formed during the first step deposition, the crystallization of $FAPbI_3$ is more readily achieved through insertion of FAI into PbI_2 crystals. Figure 1b shows the X-ray diffraction (XRD) patterns of $FAPbI_3$ layers prepared through the two-step synthesis method. The as-synthesized $FAPbI_3$ layer without annealing treatment (denoted as RT) exhibits the pattern of "α-phase $FAPbI_3$", but shows an anomalous color of light yellow. With post-annealing at 100 and 150 °C, the color of $FAPbI_3$ layers changes to brown and dark yellow respectively, whereas the XRD pattern remains approximately identical with the RT prepared one. When further increasing the annealing temperature to 190 °C, the $FAPbI_3$ layer shows the normal black color of α-phase $FAPbI_3$. (Figure S1 presents the color evolution of the $FAPbI_3$ layer annealed at 190 °C. The color changes from

DOI: 10.1021/acs.jpcc.6b10730
J. Phys. Chem. C 2016, 120, 26710−26719

yellow to brown and to light brown, and then the color begins to darken.) Comparing the XRD patterns of $FAPbI_3$ layers at different annealing temperatures, the $FAPbI_3$ black polymorph derived by annealing at 190 °C shows a stronger (110) preferred orientation than the "α-phase $FAPbI_3$" prepared at temperature below 150 °C, and the intensity ratio of the (220) peak to the (202) peak is increased from ~1 to ~3.2 after the color changes from yellow to black. Figure S2 shows the UV–vis absorption spectra of $FAPbI_3$ layers prepared at different annealing temperatures. The $FAPbI_3$ black polymorph with 190 °C annealing exhibits the absorption edge at ~821 nm, while the $FAPbI_3$ layers annealed at RT, 100 and 150 °C show an obvious blue shift of the absorption edge, and a decrease of the absorption coefficient in the whole range. Figure 1c presents the XRD of $FAPbI_3$ layers after storage in ambient air (50% humidity) for 4 days. The color of $FAPbI_3$ layers prepared at temperature below 150 °C changed to bright yellow, while the XRD patterns still remain the same. For the $FAPbI_3$ black polymorph obtained at 190 °C annealing, the $FAPbI_3$ non-perovskite polymorph (δ-phase) begins to emerge owing to the transition from perovskite α-phase to non-perovskite δ-phase. This result leads toward the conclusion that the yellow $FAPbI_3$ layer prepared by annealing below 150 °C may be an intermediate state during the phase evolution. Understanding the origin of the intermediate phase needs more in-depth studies. In PSCs, the $FAPbI_3$ black polymorph is required to work as the light absorber, and the formation of δ-phase $FAPbI_3$ or any other intermediate phase should be avoided. From the results, it can be deduced that, through two-step synthesis between PbI_2 and FAI, sufficient thermal energy is required for the formation of the $FAPbI_3$ black polymorph.

Perovskite crystallization can be induced by external stimuli, e.g., electrical field, temperature, or pressure,[20−23] or internal stimuli where the reactant materials also could affect the crystallization kinetics. Here, we exploited the modification of the PbI_2 crystal structure to modulate the crystallization of $FAPbI_3$ perovskites. PbI_2 adopts a two-dimensional (2D) layered hexagonal structure. Each stacking layer is composed of octahedrally arranged lead ions, sandwiched between two sheets of iodide ions. The sequence of the I-Pb-I plane forms a molecular layer, and the adjacent molecular layers are bonded by weak van der Waals interaction.[24,25] Consequently, the foreign molecule could be easily intercalated between the adjacent I-Pb-I layers. Inspired by the work of Jo et al.,[26] we utilized the solvents dimethyl sulfoxide (DMSO) and *N*-methyl-2-pyrrolidone (NMP) as the guest molecules to intercalate into the I-Pb-I layers via a solution-based method. Figure 2a shows the XRD patterns of pristine PbI_2 film, PbI_2(DMSO) film prepared via PbI_2(DMSO) powder, PbI_2-DMSO film, and PbI_2-NMP film prepared via the solution-based method. The pristine PbI_2 film shows (001) diffraction peaks at 12.7° with lattice constant a of 4.56 Å and c of 6.98 Å.[27] The intercalation of guest molecules in PbI_2 layers leads to lattice expansion along the c-axis. The (001) diffraction peaks of PbI_2(DMSO) film and PbI_2-DMSO film are shifted to 9.8°, and the calculated distance along the c-axis is increased to 9.04 Å. The result verifies the successful intercalation of DMSO into the PbI_2 lattice by the solution-based method. When DMSO is replaced with NMP, due to the larger size of NMP, the (001) peak of the PbI_2-NMP complex is further shifted down to 8.1°, and the distance along the c-axis is increased to 10.94 Å. In addition, we observed a small amount of pristine PbI_2 with the diffraction peak at 12.7° in PbI_2(DMSO) complex film. However, for the PbI_2 complex synthesized via the solution-based method, PbI_2-DMSO and PbI_2-NMP show no pristine PbI_2 peak, revealing the reproducible preparation of the PbI_2 complex. Figure S3 lists the physical dimensions and molecular model images of DMSO and NMP. In DMSO, the distance of C1–S1 and C2–S1 is 1.809 Å, and the O1–S1 distance is 1.50 Å. The lattice expansion (Δc) of the PbI_2-DMSO complex is 2.06 Å. Owing to the molecular rotation and van der Waals bonding, the dimensions of DMSO are comparable to the lattice expansion. For NMP, the distances of C5–C1 and C5–C3 present the longest dimensions of NMP, which are 3.70 and 3.74 Å, respectively. The lattice expansion (Δc) of the PbI_2-NMP complex is 3.96 Å. The dimension of NMP exactly matches the lattice expansion of the PbI_2-NMP complex. As the intercalation process is a topotatic reaction, the pristine layered structure should be recovered by the deintercalation process. Figure S4 shows the pictures of the samples, UV–vis absorption spectra, XRD of the PbI_2-NMP complex, and PbI_2-NMP after deintercalation. The PbI_2-NMP complex shows the light yellow color, whereas, after deintercalation, the color changed to bright yellow (Figure S4a). From the UV–vis absorption spectra, it is observed that, after deintercalation, the absorption turns back to that of pristine PbI_2, showing an absorption edge at ~520 nm (Figure S4b). As shown in Figure S4c, the (001) diffraction peak of the PbI_2-NMP complex is located at 8.1°, whereas, after the deintercalation process, the (001) peak moves to 12.7°. The PbI_2 complex could be recovered to pristine PbI_2 after deintercalation, which further confirms the intercalation of the NMP in PbI_2 lattice.

Figure 2b shows the UV–vis absorption spectra of pristine PbI_2 film and PbI_2 complex films. The pristine PbI_2 film shows an absorption edge around 520 nm, whereas, after the intercalation of the DMSO molecule, the absorption onset shows a blue shift, and the intercalation of the NMP molecule can further shift the absorption edge to lower wavelength. Lattice strain was demonstrated to be an effective way to tailor the optical properties of 2D layered material.[28−31] Volumetric strain can be caused by the bond distance change in a crystal lattice. In the PbI_2 complex, the expansion along the [001] direction generates a uniaxial tensile strain in the PbI_2 crystal lattice, and the lattice strain could be enhanced by enlarging the size of the guest molecule. The conduction band of PbI_2 is determined by p_z states, and the valence band corresponds to I s and p states and Pb s states.[32] The lattice strain induced by expansion would cause dislocations in the crystal and hence perturb the spin–orbit coupling of I-Pb-I, resulting in the band-shifting of the PbI_2 complex. To further confirm the existence of lattice strain in the PbI_2 complex, Raman spectroscopy was performed (Figure S5). We chose the pristine PbI_2 and its complex with larger lattice strain (PbI_2-NMP) for comparison. PbI_2 employed for PSC synthesis belongs to the 2H polytype giving rise to four vibrational modes, which are symmetric stretch (A_{1g}), doubly degenerate (E_g), asymmetric stretch (A_{2u}), and bend (E_u), respectively.[33,34] The pristine PbI_2 shows bands at 91, 104, and 213 cm^{-1}, which can be attributed to A_{1g}, E_u, and A_{2u} modes, respectively.[35,36] Compared with pristine PbI_2, there is a red shift of A_{1g} with $\Delta\omega$ = 5 cm^{-1} and a blue shift of the E_u mode with $\Delta\omega$ = 3 cm^{-1} observed for the PbI_2-NMP complex. Upon NMP intercalation, there is lattice expansion along the [001] direction. Compared with pristine PbI_2, the corresponding structure expansion and the stacking sequence disruption in PbI_2-NMP will cause lattice strain, and that will alter the PbI_2 vibration and result in band-shifting.

DOI: 10.1021/acs.jpcc.6b10730
J. Phys. Chem. C 2016, 120, 26710−26719

Here, the Raman band-shifting with NMP intercalation confirms the induced lattice strain in the PbI_2 complex.

As discussed above, $FAPbI_3$ perovskites have both the black perovskite polymorph (α-$FAPbI_3$) and the yellow non-perovskite polymorph (δ-$FAPbI_3$), or they could exist as an intermediate phase. δ-$FAPbI_3$ exists as a 1D chainlike structure with hexagonal symmetry. Upon annealing at the temperature of 150−160 °C, a phase transition occurs from 1D non-perovskite phase to 3D pseudocubic perovskite phase.[6,37] Herein, we found that the crystal structure of PbI_2 could affect the formation of $FAPbI_3$ perovskites. Figure 2c shows the XRD of $FAPbI_3$ perovskites synthesized by PbI_2-DMSO, PbI_2-NMP reacting with FAI, and the mixed composition $FAPbI_3$ perovskite by treating the PbI_2-NMP film with FAI/MABr mixed solution (molar ratio of FAI to MABr is 85:15, denoted as MIX-$FAPbI_3$), after a post-annealing process at 100 °C for 10 min. The XRD pattern of the $FAPbI_3$ layer synthesized with PbI_2-DMSO is dominated by the diffraction from the non-perovskite δ-$FAPbI_3$ phase. For PbI_2-NMP, the peaks attributed to the perovskite α-$FAPbI_3$ phase notably increased relative to δ-$FAPbI_3$. This implies that compared with PbI_2-DMSO, PbI_2-NMP is more favorable toward the crystallization of α-$FAPbI_3$ perovskite.

For the synthesis of α-$FAPbI_3$ black perovskite, the reaction between PbI_2 and FAI needs to overcome the energy barrier of the intermediate state to reach the final product. In the case of pristine PbI_2, thermal activation with a temperature of 190 °C is required to overcome the energy barrier (Figure 1b). For the PbI_2 complex, with the evaporation of the intercalated solvent in I-Pb-I layers, the strain energy in PbI_2 crystals will be released. The released strain energy could raise the system's internal energy and reduce the energy barrier for the crystallization of α-$FAPbI_3$ perovskite, as illustrated in Figure 2d. Owing to higher lattice strain, induced with the intercalation of NMP, the larger strain energy in PbI_2-NMP will facilitate the crystallization of α-$FAPbI_3$ perovskites. Assisted by the PbI_2-NMP complex, the crystallization of α-$FAPbI_3$ perovskite is favored. We further utilized composition engineering by replacing 15 mol % FAI with MABr for stabilization. It is observed that δ-$FAPbI_3$ is completely suppressed after annealing at 100 °C and only peaks attributed to the α-$FAPbI_3$ perovskite structure are present in the XRD spectrum, as shown in Figure 2c. The stabilization of the $FAPbI_3$ black polymorph by composition engineering could be ascribed to tuning the tolerance factor to a smaller value.[14]

Figure 3a,b shows the top-view SEM of the PbI_2-NMP layer and the MIX-$FAPbI_3$ layer prepared by PbI_2-NMP. The PbI_2-NMP layer is composed of uniformly distributed hexagonal-shaped nanoplates. The formation of anisotropic nanoplates is related to the hexagonally packed I-Pb-I layer. Owing to the low index of the basal plane, the PbI_2 crystal grows faster along in-plane directions compared to the *c*-axis direction.[38−40] The loosely aligned hexagonal nanoplates are beneficial for FAI solution penetration, thus assisting the formation of $FAPbI_3$-based perovskite. As shown in Figure 3b, the MIX-$FAPbI_3$ film derived from PbI_2-NMP exhibits a dense and well-formed grain structure with a grain size around 300 nm. Figure 3c shows the cross-sectional SEM of MIX-$FAPbI_3$ film deposited on the low temperature processed TiO_2 compact layer. The thickness of the TiO_2 compact layer and perovskite layer is approximately 90 and 500 nm, respectively. To elucidate the optical property of the mixed composition perovskite, herein, we compare the UV−vis absorption spectra of $MAPbI_3$, $FAPbI_3$, and MIX-

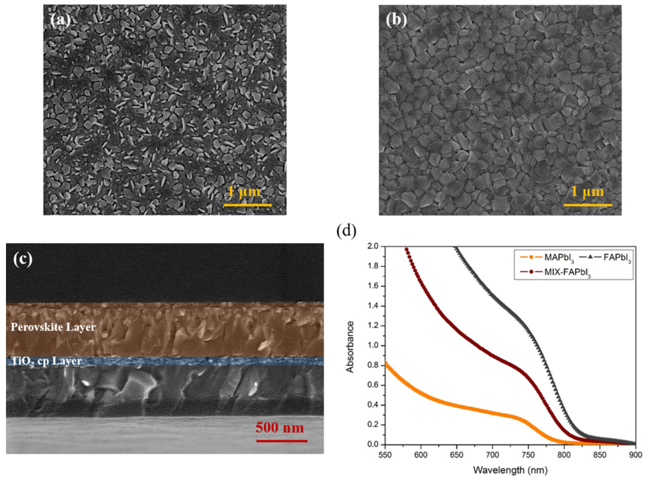

Figure 3. (a) Top-view SEM of PbI_2-NMP complex layer. (b) Top-view SEM of mixed composition $FAPbI_3$ perovskite layer. (c) Cross-sectional SEM of mixed composition $FAPbI_3$ perovskite deposited on low temperature solution processed TiO_2 compact layer. (d) UV−vis absorption spectra of $MAPbI_3$, $FAPbI_3$, and mixed composition $FAPbI_3$ perovskite layer.

$FAPbI_3$ film as shown in Figure 3d. $FAPbI_3$ and MIX-$FAPbI_3$ perovskite are prepared through the PbI_2-NMP complex, which is annealed at 150 and 100 °C to obtain pure α-$FAPbI_3$. The calculated band gap of $MAPbI_3$ and $FAPbI_3$ is 1.57 and 1.51 eV, respectively. For MIX-$FAPbI_3$, the absorption is slightly blue-shifted, delivering a band gap of 1.53 eV.

Motivated by the feasibility of the low temperature solution-based fabrication process for $FAPbI_3$ perovskites, we explored the low temperature synthesis of the perovskite solar cell with n-i-p architecture, as illustrated in Figure 4a. In this structure, the TiO_2 compact layer was synthesized by spin-coating binder-free TiO_2 slurry on FTO glass. The TiO_2 slurry is composed of volatile solvents and nano-TiO_2 sol particles. During drying at room temperature, owing to the dehydration process among surface hydroxyl, closely interconnected TiO_2 nanoparticles with high density were formed on the FTO glass substrate, as shown in Figure S6a, which presents the top-view SEM image of the TiO_2 compact layer. From the cross-sectional SEM image of the TiO_2 compact layer (Figure S6b), it is observed that the thickness of the TiO_2 compact layer is ∼90 nm, ensuring hole block and electron transport. Figure 4b,c displays the atomic force microscopy (AFM) images of the FTO glass substrate and TiO_2 compact layer/FTO glass. As TiO_2 conformably fills the unleveled FTO crystal, the root-mean-square (RMS) roughness decreases from 29.8 to 13.2 nm upon the deposition of the low temperature TiO_2 compact layer on FTO glass. The smooth TiO_2 surface enables the growth of a uniform and compact perovskite layer. Figure 4d presents the optical transmission spectra of FTO glass and TiO_2 compact layer/FTO glass. It can be noted that the transparency of TiO_2 compact layer/FTO glass is higher than that of empty FTO glass over the visible light range. The result further confirms the smooth surface of the TiO_2 compact layer, which reduces the light reflection, and leads to the increase of light transmission. The high transparency window substrate allows the perovskite layer to absorb more light and generate photoelectrons.

Besides the optical property, high crystallinity of the TiO_2 compact layer could facilitate the electron transport and hence improve the photovoltaic performance of the solar cell. Figure

DOI: 10.1021/acs.jpcc.6b10730
J. Phys. Chem. C 2016, 120, 26710−26719

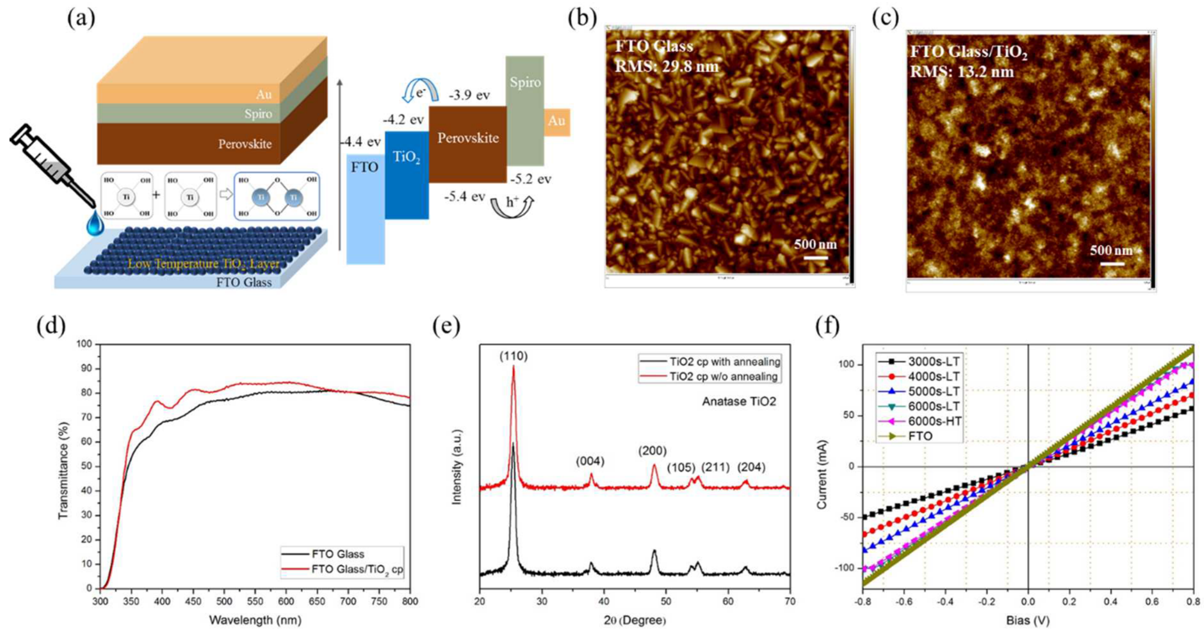

Figure 4. (a) Schematic representation and energy level diagram of perovskite solar cell based on low temperature solution processed TiO_2 compact layer. AFM images of (b) FTO glass substrate and (c) TiO_2 compact layer/FTO glass. (d) Transmittance spectra of FTO glass substrate and TiO_2 compact layer/FTO glass. (e) XRD of low temperature solution processed TiO_2 compact layer with and without annealing. (f) Linear sweep voltammetry of TiO_2 compact layer synthesized at different spin speeds.

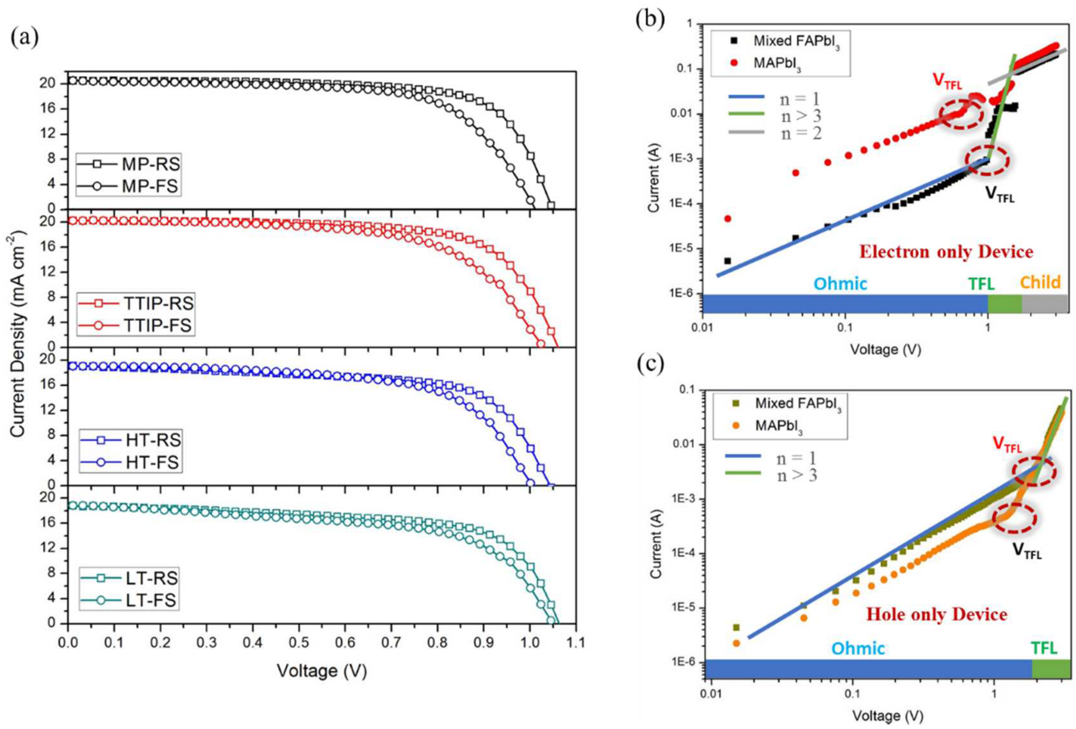

Figure 5. (a) *J*−*V* curves of MP cell, TTIP cell, HT cell, and LT cell recorded through reverse-scan (RS) and forward-scan (FS). Current−voltage curve for (b) electron transport-only device and (c) hole transport-only device.

4e shows the XRD of the low temperature solution processed TiO_2 compact layer with and without high temperature annealing. The low temperature synthesized TiO_2 compact layer shows pure anatase phase. With an additional annealing process at 500 °C for 1 h, the XRD pattern still remains identical, indicating high crystallinity of the TiO_2 compact layer obtained by the low temperature solution process. In order to evaluate electron transport property of the low temperature processed TiO_2 compact layer, linear sweep voltammetry (LSV) of the FTO glass/TiO_2 compact layer/Au device was measured, as shown in Figure 4f. The linear increase of current with applied potential indicates Ohmic response of the TiO_2 compact layer. We vary the thickness of the TiO_2 layer via adjusting spinning speed, through which film thickness decreases with the increase of spinning speed. In the case of poor quality TiO_2 film with pinholes, the thermally evaporated

DOI: 10.1021/acs.jpcc.6b10730
J. Phys. Chem. C 2016, 120, 26710−26719

Au electrode will contact the FTO glass, which will result in identical voltage−current response between the TiO_2 compact layer and FTO glass. Here, the current difference between the TiO_2 compact layer and FTO glass, coupled with the dependence of current with film thickness, suggests a high density and pinhole-free TiO_2 layer obtained through the low temperature solution process. The high temperature annealing process not only facilitates TiO_2 crystal formation but also enhances TiO_2 nanoparticle interconnection, which is believed to improve electron transport through TiO_2 compact layer. In order to demonstrate the annealing effect on electron transport property, we compare the LSV of the TiO_2 layer synthesized at 6000 rpm, with and without high temperature annealing. It is observed that the voltage−current response of the TiO_2 compact layer does not change with additional annealing processes, implying that the low temperature solution processed TiO_2 compact layer exhibits high nanoparticle interconnection and favorable electron transport property.

To elucidate the influence of the electron transport layer on the photovoltaic performance of MIX-$FAPbI_3$ PSC, four different device architectures were fabricated. One is the mesoporous device (denoted as MP) employing mesoporous TiO_2 (mp-TiO_2) as the electron transport layer, which is synthesized through our previously reported method.[41] The other three are planar devices which differ in the synthesis method for the TiO_2 compact layer, as shown in the schematic drawings of device architectures (Figure S7). The device denoted as TTIP utilizes TiO_2 film synthesized by hydrolysis of titanium isopropoxide (TTIP), followed by annealing at 500 °C as the electron transport compact layer. The HT and LT devices employ a low temperature solution processed TiO_2 compact layer, which are treated with and without the high temperature annealing process, respectively. Figure 5a presents the current density−voltage (J−V) curves with different scan directions for the four types of solar cells under simulated 1 sun (AM 1.5G). The corresponding photovoltaic parameters are listed in Table 1. The MP solar cell using mp-TiO_2 as electron transport layer exhibits the highest fill factor among the four types of solar cells. In the mesoporous architecture solar cell, due to the penetration of perovskites into TiO_2 mesoporous film, the contact resistance between perovskite and TiO_2 is smaller compared to the planar solar cell, thus leading to higher fill factor. The hysteresis in the J−V curves of PSC with respect to the different scan direction complicates the conversion efficiency determination. Normally, due to the promoted electron transport through mesoporous TiO_2 film, the mesoporous PSC has less hysteresis in J−V curves as compared to planar solar cells.[42,43] The MP PSC shows a reverse-scan (RS) efficiency of 15.5% and a forward-scan (FS) efficiency of 13.7%, whereas, for the planar TTIP solar cell, it exhibits 15.0% RS efficiency and 13.0% FS efficiency. The difference in the RS efficiency and FS efficiency is similar between mesoporous and planar architectures. This implies that the MIX-$FAPbI_3$ perovskite would have more balanced electron and hole transport that could favor the reduction of hysteresis.[11] Further, we replaced the conventional TiO_2 compact layer derived from TTIP with our low temperature solution processed TiO_2 compact layer. The HT solar cell shows RS efficiency of 13.2% and FS efficiency of 12.0%, whereas the LT solar cell shows RS efficiency of 13.2% and FS efficiency of 11.8%. The histogram of conversion efficiency of the LT solar cell derived from 30 samples is summarized in Figure S8. More than 70% of cells yield a conversion efficiency over 12.5%, and the average efficiency of the low temperature perovskite cell is 13.0% ± 0.3%, indicating high reproducibility in fabrication of the LT perovskite solar cell. The comparable photovoltaic performance between HT and LT solar cells indicates that an efficient charge transport process occurred in the low temperature solution processed TiO_2 compact layer, and the high temperature annealing process could hardly further improve its photovoltaic performance. Figure S9 shows the J−V curves of PSC fabricated by PbI_2-DMSO. The cell shows RS efficiency of 12.7% and FS efficiency of 10.3%, which is lower than that of PbI_2-NMP. As PbI_2-NMP has higher lattice strain than PbI_2-DMSO, PbI_2-NMP facilitates the formation of the $FAPbI_3$ black polymorph. The high-quality $FAPbI_3$-based perovskite layer synthesized by PbI_2-NMP results in improved performance.

Table 1. Photovoltaic Parameters for MP Cell, TTIP Cell, HT Cell, and LT Cell

solar cells	V_{oc} (V)	J_{sc} (mA cm^{-2})	FF	efficiency (%)
MP-RS	1.04	20.54	0.72	15.5
MP-FS	1.01	19.72	0.66	13.7
TTIP-RS	1.06	20.23	0.70	15.0
TTIP-FS	1.02	20.24	0.62	13.0
HT-RS	1.04	19.10	0.66	13.2
HT-FS	1.05	18.94	0.63	12.0
LT-RS	1.06	18.79	0.66	13.2
LT-FS	1.04	18.76	0.60	11.8

To reveal the origin of reduced hysteresis in MIX-$FAPbI_3$ PSC, a control experiment using $MAPbI_3$ perovskite as the light absorber was also conducted. Figure S10 shows the RS and FS J−V curves of the low temperature $MAPbI_3$ perovskite solar cell. In contrast, the $MAPbI_3$ perovskite shows severe hysteresis, with RS efficiency of 12.4% and FS efficiency of 4.53%. The differences mainly arise from the decline of open circuit voltage and fill factor. Except for the perovskite layer, all other components between $MAPbI_3$ and MIX-$FAPbI_3$ PSC are identical. This indicates that the suppressed hysteresis is more likely coming from the intrinsic carrier transport property of the mixed composition $FAPbI_3$ perovskites.

Regarding the underlying mechanism of hysteresis in PSC, the charge trapping and detrapping process in bulk or at the interface of perovskite has been suggested as a possible reason.[42,44−46] Here, we estimate carrier trap density of the mixed composition $FAPbI_3$ perovskite through space-charge limited current (SCLC) measurements. In order to obtain both electron and hole trap density, an electron transport-only device and a hole transport-only device were constructed by sandwiching the perovskite layer with electron transport layers (PCBM) and hole transport layers (Spiro-OMeTAD), respectively.[47] As presented in Figure 5b,c, the I−V plot of SCLC can be separated into different response regions. At low voltage, the current is linearly proportional to the applied voltage, which corresponds to Ohmic response. At higher voltage, the applied voltage results in the formation of a trap-filled limit (TFL) region, where all the available trap states were filled by the injected carriers.[48,49] The voltage V_{TFL} is linearly proportional to the density of trap states, which can be expressed through eq 1[49,50]

$$V_{TFL} = eN_tL^2/2\varepsilon\varepsilon_0 \quad (1)$$

where e is the electron charge, N_t is the trap density, L is the thickness of perovskite film, ε_0 is the vacuum permittivity, and ε

DOI: 10.1021/acs.jpcc.6b10730
J. Phys. Chem. C 2016, 120, 26710−26719

is the relative dielectric constant of the perovskite layer. The value of ε is found to be 32 for $MAPbI_3$ perovskite[47] and 49.4 for $FAPbI_3$-based perovskite.[51,52] The electron trap density N_{et} for $MAPbI_3$ perovskite was calculated to be 3.62×10^{16} cm^{-3}, and for $FAPbI_3$-based perovskite, it was found to be 2.14×10^{16} cm^{-3}. Similarly, the hole trap density for $MAPbI_3$ perovskite was calculated to be 7.25×10^{16} cm^{-3}, and for $FAPbI_3$-based perovskite, it was found to be 4.11×10^{16} cm^{-3}. It is noted that compared with $MAPbI_3$, the $FAPbI_3$-based perovskite shows both lower electron trap density and hole trap density. Traps in perovskite are crucial for the carrier life, and the decreased trap density in $FAPbI_3$-based perovskite could enhance charge extraction.[45,46] This may be one of the possible reasons explaining the suppressed hysteresis of mixed composition $FAPbI_3$ PSC.

4. CONCLUSION

In terms of crystallization of the $FAPbI_3$ black polymorph, we found the intercalation of solvent between the adjacent I-Pb-I layers causes lattice strain in the PbI_2 crystal, and the induced strain energy could reduce the barrier for the intermediate state which favors the crystallization of the black $FAPbI_3$ polymorph. Owing to the larger size of NMP compared with DMSO, the PbI_2-NMP complex exhibits higher lattice strain and is more favorable to the formation of the α-$FAPbI_3$ phase. With the utilization of the PbI_2-NMP complex and incorporation of MABr in FAI, the black polymorph of mixed composition $FAPbI_3$ was synthesized. A low temperature solution-based process was developed to synthesize the TiO_2 compact layer. The low temperature processed TiO_2 shows good crystallinity, high optical transmission, and superior electron transport property, which is found to be positive toward improving PSC photovoltaic performance. The low temperature mixed composition $FAPbI_3$ perovskite solar cell shows 13.2% RS efficiency and 11.8% FS efficiency. In comparison to $MAPbI_3$ perovskite, the lower electron and hole trap state density in the mixed composition $FAPbI_3$ perovskite could account for the reduced hysteresis. The study demonstrates a new perspective toward modulating the crystallization kinetics of the black $FAPbI_3$ polymorph and also provides a cost-effective method for preparing the low temperature perovskite solar cell.

■ ASSOCIATED CONTENT

Supporting Information

The Supporting Information is available free of charge on the ACS Publications website at DOI: 10.1021/acs.jpcc.6b10730.

> Experimental details; color evolution of $FAPbI_3$ layer; UV–vis absorption spectra of the $FAPbI_3$ layers; physical dimensions of DMSO and NMP; UV–vis absorption spectra and XRD of PbI_2-NMP with and without deintercalation; Raman spectra comparison between pristine PbI_2 and PbI_2-NMP complex; SEM of low temperature solution processed TiO_2 compact layer; structure illustration of MP cell, TTIP cell, HT cell, and LT cell; histogram of conversion efficiency for 30 perovskite solar cells; J–V curves of low temperature perovskite solar cell prepared by PbI_2-DMSO; and J–V curves of low temperature $MAPbI_3$ perovskite solar cell (PDF)

■ AUTHOR INFORMATION

Corresponding Authors

*E-mail: spriya@vt.edu. Tel: 540-231-0745 (S.P.).
*E-mail: ccw39@vt.edu. Tel: 540-750-3959 (C.W.).
*E-mail: xiaojia@vt.edu. Tel: 540-808-6997 (X.Z.).

Notes

The authors declare no competing financial interest.

■ ACKNOWLEDGMENTS

The authors acknowledge the financial support from the Institute of Critical Technology and Applied Science (ICTAS). Authors S.P. and Q.Y. would like to acknowledge the financial support from the Office of Naval Research through the MURI program. Y.Y. was supported through the Office of Naval Research participation in NSF I/UCRC: Center for Energy Harvesting Materials and Systems (CEHMS). The authors thank Dr. Bob Bodnar and Charles Farley, Department of Geosciences, Virginia Tech, for Raman spectroscopy assistance.

■ REFERENCES

(1) Kim, H. S.; Lee, C. R.; Im, J. H.; Lee, K. B.; Moehl, T.; Marchioro, A.; Moon, S. J.; Humphry-Baker, R.; Yum, J. H.; Moser, J. E.; et al. Lead Iodide Perovskite Sensitized All-Solid-State Submicron Thin Film Mesoscopic Solar Cell with Efficiency Exceeding 9%. *Sci. Rep.* **2012**, *2*, 591.

(2) Snaith, H. J. Perovskites: The Emergence of a New Era for Low-Cost, High-Efficiency Solar Cells. *J. Phys. Chem. Lett.* **2013**, *4*, 3623–3630.

(3) Stranks, S. D.; Snaith, H. J. Metal-Halide Perovskites for Photovoltaic and Light-Emitting Devices. *Nat. Nanotechnol.* **2015**, *10*, 391–402.

(4) Conings, B.; Drijkoningen, J.; Gauquelin, N.; Babayigit, A.; D'Haen, J.; D'Olieslaeger, L.; Ethirajan, A.; Verbeeck, J.; Manca, J.; Mosconi, E.; et al. Intrinsic Thermal Instability of Methylammonium Lead Trihalide Perovskite. *Adv. Energy Mater.* **2015**, *5*, 1500477.

(5) Zheng, X.; Chen, B.; Yang, M.; Wu, C.; Orler, B.; Moore, R. B.; Zhu, K.; Priya, S. The Controlling Mechanism for Potential Loss in $CH_3NH_3PbBr_3$ Hybrid Solar Cells. *ACS Energy Lett.* **2016**, *1*, 424–430.

(6) Stoumpos, C. C.; Malliakas, C. D.; Kanatzidis, M. G. Semiconducting Tin and Lead Iodide Perovskites with Organic Cations: Phase Transitions, High Mobilities, and Near-Infrared Photoluminescent Properties. *Inorg. Chem.* **2013**, *52*, 9019–9038.

(7) Pellet, N.; Gao, P.; Gregori, G.; Yang, T. Y.; Nazeeruddin, M. K.; Maier, J.; Grätzel, M. Mixed-Organic-Cation Perovskite Photovoltaics for Enhanced Solar-Light Harvesting. *Angew. Chem., Int. Ed.* **2014**, *53*, 3151–3157.

(8) Koh, T. M.; Fu, K.; Fang, Y.; Chen, S.; Sum, T. C.; Mathews, N.; Mhaisalkar, S. G.; Boix, P. P.; Baikie, T. Formamidinium-Containing Metal-Halide: An Alternative Material for near-IR Absorption Perovskite Solar Cells. *J. Phys. Chem. C* **2014**, *118*, 16458–16462.

(9) Eperon, G. E.; Stranks, S. D.; Menelaou, C.; Johnston, M. B.; Herz, L. M.; Snaith, H. J. Formamidinium of Formamidinium Lead Trihalide: A Broadly Tunable Perovskite for Efficient Planar Heterojunction Solar Cells. *Energy Environ. Sci.* **2014**, *7*, 982.

(10) Lee, J. W.; Kim, D. H.; Kim, H. S.; Seo, S. W.; Cho, S. M.; Park, N. G. Formamidinium and Cesium Hybridization for Photo- and Moisture-Stable Perovskite Solar Cell. *Adv. Energy Mater.* **2015**, *5*, 1501310.

(11) Jeon, N. J.; Noh, J. H.; Yang, W. S.; Kim, Y. C.; Ryu, S.; Seo, J.; Seok, S. Il. Compositional Engineering of Perovskite Materials for High-Performance Solar Cells. *Nature* **2015**, *517*, 476–480.

(12) Wang, Z.; Zhou, Y.; Pang, S.; Xiao, Z.; Zhang, J.; Chai, W.; Xu, H.; Liu, Z.; Padture, N. P.; Cui, G. Additive-Modulated Evolution of $HC(NH_2)_2PbI_3$ Black Polymorph for Mesoscopic Perovskite Solar Cells. *Chem. Mater.* **2015**, *27*, 7149–7155.

DOI: 10.1021/acs.jpcc.6b10730
J. Phys. Chem. C 2016, 120, 26710–26719

(13) Binek, A.; Hanusch, F. C.; Docampo, P.; Bein, T. Stabilization of the Trigonal High-Temperature Phase of Formamidinium Lead Iodide. *J. Phys. Chem. Lett.* **2015**, *6*, 1249−1253.
(14) Li, Z.; Yang, M.; Park, J. S.; Wei, S. H.; Berry, J. J.; Zhu, K. Stabilizing Perovskite Structures by Tuning Tolerance Factor: Formation of Formamidinium and Cesium Lead Iodide Solid-State Alloys. *Chem. Mater.* **2016**, *28*, 284−292.
(15) Liang, P. W.; Liao, C. Y.; Chueh, C. C.; Zuo, F.; Williams, S. T.; Xin, X. K.; Lin, J.; Jen, A. K. Y. Additive Enhanced Crystallization of Solution-Processed Perovskite for Highly Efficient Planar-Heterojunction Solar Cells. *Adv. Mater.* **2014**, *26*, 3748−3754.
(16) Wang, F.; Yu, H.; Xu, H.; Zhao, N. $HPbI_3$: A New Precursor Compound for Highly Efficient Solution-Processed Perovskite Solar Cells. *Adv. Funct. Mater.* **2015**, *25*, 1120−1126.
(17) Yang, W. S.; Noh, J. H.; Jeon, N. J.; Kim, Y. C.; Ryu, S.; Seo, J.; Seok, S. Il. High-Performance Photovoltaic Perovskite Layers Fabricated through Intramolecular Exchange. *Science* **2015**, *348*, 1234−1237.
(18) Kim, B. J.; Kim, D. H.; Lee, Y. Y.; Shin, H. W.; Han, G. S.; Hong, J. S.; Mahmood, K.; Ahn, T.; Joo, Y. C.; Hong, K. S.; et al. Highly Efficient and Bending Durable Perovskite Solar Cells: Toward Wearable Power Source. *Energy Environ. Sci.* **2015**, *8*, 916−921.
(19) Yang, D.; Yang, R.; Zhang, J.; Yang, Z.; Liu, S.; Li, C. High Efficiency Flexible Perovskite Solar Cells Using Superior Low Temperature TiO_2. *Energy Environ. Sci.* **2015**, *8*, 3208−3214.
(20) Frost, J. M.; Butler, K. T.; Brivio, F.; Hendon, C. H.; Van Schilfgaarde, M.; Walsh, A. Atomistic Origins of High-Performance in Hybrid Halide Perovskite Solar Cells. *Nano Lett.* **2014**, *14*, 2584−2590.
(21) Lee, Y.; Mitzi, D.; Barnes, P.; Vogt, T. Pressure-Induced Phase Transitions and Templating Effect in Three-Dimensional Organic-Inorganic Hybrid Perovskites. *Phys. Rev. B: Condens. Matter Mater. Phys.* **2003**, *68*, 020103.
(22) Jacobsson, T. J.; Schwan, L. J.; Ottosson, M.; Hagfeldt, A.; Edvinsson, T. Determination of Thermal Expansion Coefficients and Locating the Temperature-Induced Phase Transition in Methylammonium Lead Perovskites Using X-Ray Diffraction. *Inorg. Chem.* **2015**, *54*, 10678−10685.
(23) Jiang, S.; Fang, Y.; Li, R.; Xiao, H.; Crowley, J.; Wang, C.; White, T. J.; Goddard, W. A.; Wang, Z.; Baikie, T.; et al. Pressure-Dependent Polymorphism and Band-Gap Tuning of Methylammonium Lead Iodide Perovskite. *Angew. Chem., Int. Ed.* **2016**, *55*, 6540−6544.
(24) Ogawa, M.; Kuroda, K. Photofunctions of Intercalation Compounds. *Chem. Rev.* **1995**, *95*, 399−438.
(25) Coleman, C. C.; Goldwhite, H.; Tikkanen, W. A Review of Intercalation in Heavy Metal Iodides. *Chem. Mater.* **1998**, *10*, 2794−2800.
(26) Jo, Y.; Oh, K. S.; Kim, M.; Kim, K. H.; Lee, H.; Lee, C. W.; Kim, D. S. High Performance of Planar Perovskite Solar Cells Produced from PbI_2(DMSO) and PbI_2(NMP) Complexes by Intramolecular Exchange. Advanced Materials Interfaces. *Adv. Mater. Interfaces* **2016**, *3*, 1500768.
(27) Pałosz, B.; Salje, E. Lattice Parameters and Spontaneous Strain in AX_2 Polytypes: CdI_2, PbI_2 SnS_2 and $SnSe_2$. *J. Appl. Crystallogr.* **1989**, *22*, 622−623.
(28) Zhou, M.; Duan, W.; Chen, Y.; Du, A. Single Layer Lead Iodide: Computational Exploration of Structural, Electronic and Optical Properties, Strain Induced Band Modulation and the Role of Spin-orbital-Coupling. *Nanoscale* **2015**, *7*, 15168−15174.
(29) Yang, L.; Cui, X.; Zhang, J.; Wang, K.; Shen, M.; Zeng, S.; Dayeh, S. a; Feng, L.; Xiang, B. Lattice Strain Effects on the Optical Properties of MoS_2 Nanosheets. *Sci. Rep.* **2014**, *4*, 5649.
(30) Wang, Y.; Sun, Y. Y.; Zhang, S.; Lu, T. M.; Shi, J. Band Gap Engineering of a Soft Inorganic Compound PbI_2 by Incommensurate van Der Waals Epitaxy. *Appl. Phys. Lett.* **2016**, *108*, 013105.
(31) Oakes, L.; Carter, R.; Hanken, T.; Cohn, A. P.; Share, K.; Schmidt, B.; Pint, C. L. Interface Strain in Vertically Stacked Two-Dimensional Heterostructured Carbon-MoS_2 Nanosheets Controls Electrochemical Reactivity. *Nat. Commun.* **2016**, *7*, 11796.
(32) Doni, E.; Grosso, G.; Spavieri, G. Band Structure and Absorption Edge of PbI_2. *Solid State Commun.* **1972**, *11*, 493−497.
(33) Capozzi, V.; Fontana, A.; Fontana, M. P.; Mariotto, G.; Montagna, M.; Viliani, G. Raman Scattering in PbI_2. *Nuovo Cim. B* **1977**, *39*, 556−560.
(34) Khilji, M. Y.; Sherman, W. F.; Wilkinson, G. R. Raman Study of Three Polytypes of PbI_2. *J. Raman Spectrosc.* **1982**, *13*, 127−133.
(35) Sears, W.; Klein, M.; Morrison, J. Polytypism and the Vibrational Properties of PbI_2. *Phys. Rev. B: Condens. Matter Mater. Phys.* **1979**, *19*, 2305−2313.
(36) Nakashima, S. Raman Study of Polytypism in Vapor-Grown PbI_2. *Solid State Commun.* **1975**, *16*, 1059−1062.
(37) Koh, T. M.; Fu, K.; Fang, Y.; Chen, S.; Sum, T. C.; Mathews, N.; Mhaisalkar, S. G.; Boix, P. P.; Baikie, T. Formamidinium-Containing Metal-Halide: An Alternative Material for near-IR Absorption Perovskite Solar Cells. *J. Phys. Chem. C* **2014**, *118*, 16458−16462.
(38) Fu, F.; Kranz, L.; Yoon, S.; Löckinger, J.; Jäger, T.; Perrenoud, J.; Feurer, T.; Gretener, C.; Buecheler, S.; Tiwari, A. N. Controlled Growth of PbI_2 Nanoplates for Rapid Preparation of $CH_3NH_3PbI_3$ in Planar Perovskite Solar Cells. *Phys. Status Solidi A* **2015**, *212*, 2708−2717.
(39) Zheng, Z.; Liu, A.; Wang, S.; Wang, Y.; Li, Z.; Lau, W. M.; Zhang, L. In Situ Growth of Epitaxial Lead Iodide Films Composed of Hexagonal Single Crystals. *J. Mater. Chem.* **2005**, *15*, 4555−4559.
(40) Schieber, M.; Zamoshchik, N.; Khakhan, O.; Zuck, A. Structural Changes during Vapor-Phase Deposition of Polycrystalline-PbI_2 Films. *J. Cryst. Growth* **2008**, *310*, 3168−3173.
(41) Zheng, X.; Chen, B.; Wu, C.; Priya, S. Room Temperature Fabrication of $CH_3NH_3PbBr_3$ by Anti-Solvent Assisted Crystallization Approach for Perovskite Solar Cells with Fast Response and Small J-V Hysteresis. *Nano Energy* **2015**, *17*, 269−278.
(42) Snaith, H. J.; Abate, A.; Ball, J. M.; Eperon, G. E.; Leijtens, T.; Noel, N. K.; Stranks, S. D.; Wang, J. T.-W.; Wojciechowski, K.; Zhang, W. Anomalous Hysteresis in Perovskite Solar Cells. *J. Phys. Chem. Lett.* **2014**, *5*, 1511−1515.
(43) Kim, H. S.; Park, N. G. Parameters Affecting I-V Hysteresis of $CH_3NH_3PbI_3$ Perovskite Solar Cells: Effects of Perovskite Crystal Size and Mesoporous TiO_2 Layer. *J. Phys. Chem. Lett.* **2014**, *5*, 2927−2934.
(44) Chen, B.; Yang, M.; Priya, S.; Zhu, K. Origin of J-V Hysteresis in Perovskite Solar Cells. Journal of Physical Chemistry Letters. *J. Phys. Chem. Lett.* **2016**, *7*, 905−917.
(45) Shao, Y.; Xiao, Z.; Bi, C.; Yuan, Y.; Huang, J. Origin and Elimination of Photocurrent Hysteresis by Fullerene Passivation in $CH_3NH_3PbI_3$ Planar Heterojunction Solar Cells. *Nat. Commun.* **2014**, *5*, 5784.
(46) Wojciechowski, K.; Stranks, S. D.; Abate, A.; Sadoughi, G.; Sadhanala, A.; Kopidakis, N.; Rumbles, G.; Li, C. Z.; Friend, R. H.; Jen, A. K. Y.; et al. Heterojunction Modification for Highly Efficient Organic-Inorganic Perovskite Solar Cells. *ACS Nano* **2014**, *8*, 12701−12709.
(47) Dong, Q.; Fang, Y.; Shao, Y.; Mulligan, P.; Qiu, J.; Cao, L.; Huang, J. Electron-Hole Diffusion Lengths > 175 μm in Solution-Grown $CH_3NH_3PbI_3$ Single Crystals. *Science* **2015**, *347*, 967−970.
(48) Shi, D.; Adinolfi, V.; Comin, R.; Yuan, M.; Alarousu, E.; Buin, A.; Chen, Y.; Hoogland, S.; Rothenberger, A.; Katsiev, K.; et al. Low Trap-State Density and Long Carrier Diffusion in Organolead Trihalide Perovskite Single Crystals. *Science* **2015**, *347*, 519−522.
(49) Bube, R. H. Trap Density Determination by Space-Charge-Limited Currents. *J. Appl. Phys.* **1962**, *33*, 1733−1737.
(50) Murgatroyd, P. N. Theory of Space-Charge-Limited Current Enhanced by Frenkel Effect. *J. Phys. D: Appl. Phys.* **1970**, *3*, 151.
(51) Zhumekenov, A. A.; Saidaminov, M. I.; Haque, M. A.; Alarousu, E.; Sarmah, S. P.; Murali, B.; Dursun, I.; Miao, X. H.; Abdelhady, A. L.; Wu, T.; et al. Formamidinium Lead Halide Perovskite Crystals with Unprecedented Long Carrier Dynamics and Diffusion Length. *ACS Energy Lett.* **2016**, *1*, 32−37.
(52) Han, Q.; Bae, S. H.; Sun, P.; Hsieh, Y. T.; Yang, Y. M.; Rim, Y. S.; Zhao, H.; Chen, Q.; Shi, W.; Li, G.; et al. Single Crystal

Formamidinium Lead Iodide ($FAPbI_3$): Insight into the Structural, Optical, and Electrical Properties. *Adv. Mater.* **2016**, *28*, 2253−2258.

DOI: 10.1021/acs.jpcc.6b10730
J. Phys. Chem. C 2016, 120, 26710−26719